

**Electro-osmotic flow through nanopores in thin and ultrathin membranes**

Dmitriy V. Melnikov, Zachery K. Hulings, and Maria E. Gracheva  
*Department of Physics, Clarkson University, Potsdam, New York 13699, USA*  
 (Received 9 August 2016; published 12 June 2017)

We theoretically study how the electro-osmotic fluid velocity in a charged cylindrical nanopore in a thin solid state membrane depends on the pore's geometry, membrane charge, and electrolyte concentration. We find that when the pore's length is comparable to its diameter, the velocity profile develops a concave shape with a minimum along the pore axis unlike the situation in very long nanopores with a maximum velocity along the central pore axis. This effect is attributed to the induced pressure along the nanopore axis due to the fluid flow expansion and contraction near the exit or entrance to the pore and to the reduction of electric field inside the nanopore. The induced pressure is maximal when the pore's length is about equal to its diameter while decreasing for both longer and shorter nanopores. A model for the fluid velocity incorporating these effects is developed and shown to be in a good agreement with numerically computed results.

DOI: [10.1103/PhysRevE.95.063105](https://doi.org/10.1103/PhysRevE.95.063105)

**I. INTRODUCTION**

In recent years, nanopores in thin solid state membranes gained considerable attention due to their applications as low-cost, high-throughput biosensors and filters [1–7]. Short transit times in thin membranes for translocating biomolecules and nanoparticles as well as features in the ionic current result in high sensitivity and resolution of such devices. Signatures in the ionic current (the duration and the depth of the “current blockade” dips) are not only utilized to detect an object passing through the nanopore but they also convey information about its physical properties such as size, shape, and charge [5,8–12]. As such, understanding of how various conductance mechanisms, such as those due to membrane surface and bulk charges, affect the motion of the nanosized objects through the nanopore is of crucial importance for correct interpretation and utilization of experimental data.

When an object translocates through a nanopore, two main forces typically affect its motion [13]. The first is the electric force originating from the applied electric field that results in the electrophoretic motion of the charged nanoparticle or biomolecule. The second force is due to the viscous drag exerted on an object by the fluid flowing through the charged nanopore in response to the applied electric field, or the so called electro-osmotic flow (EOF). The EOF appears because the surface of the membrane is charged, so that the ionic solution within the nanopore attains a nonzero electric charge of opposite sign which is largely concentrated within the electric double layer formed at the walls of the nanopore. When the electric field along the axis of the pore is applied, the ions in the fluid filling the nanopore begin to move, and the fluid flow (EOF) appears. In the steady state regime, the bulk motion of the solution in the nanopore is generated (the fluid is viscous), so that the EOF is present through the total cross sectional area of the pore. Depending on the charges of the translocating object and membrane, the electric and drag forces may or may not be in one direction: For example, for a negatively charged nanoparticle attempting to permeate through a nanopore with negative surface charge, these two forces point in opposite directions. Thus, their relative magnitudes will determine the direction in which the particle translocates as well as the time it spends in the nanopore attempting to move through it. As

this time depends exponentially on the potential energy of the particle within the channel [14], even small variations in values of these forces will greatly affect the duration of the translocation event [15] and, consequently, the membrane filtering and sensing characteristics.

To this end, in this work we conduct the theoretical analysis of the EOF through nanopores in solid state thin membranes [16–19]. For this purpose, we numerically compute the fluid flow velocity through a nanopore by solving on equal footing Poisson-Nernst-Planck equations to account for the charge and electric field distributions in and around the nanopore and Navier-Stokes equations to describe the EOF. Our results show that the flow in finite length nanopores with the diameter comparable to the length cannot be adequately described by the results for the long channel with the Debye approximation [20] as this approach overestimates the fluid velocity by as much as 100%. The reason for this is the fluid flow outside the nanopore which affects the EOF through it. These “end effects” are manifested as a self-induced pressure gradient along the pore. When this effect is incorporated in the simple analytical model for the EOF velocity which we also develop on the basis of the classical model for the infinitely long nanopores [20], we find that the velocities given by this model agree very well with results of numerical calculations for a broad range of nanopore dimensions, electrolyte concentrations, and membrane surface charge densities.

The paper is structured as follows. In Sec. II, the nanopore geometry and the computational method employed are described with details on boundary conditions and parameters used in the setup of our model. In Sec. III, the results of computations are presented and discussed, the analytical model for the EOF fluid velocity is developed, and behavior of the EOF in our nanopore structure is elucidated. Finally, Sec. IV contains a brief summary of the work.

**II. MODEL AND METHODS**

In Fig. 1, a schematic diagram of our modeled membrane-electrolyte structure with the electric potential overlaid is shown. The nanopore of radius  $R_p$  and length  $L_p$  is in the center of the structure: We consider pores with  $R_p = 5$  and 10 nm while the length of the pore is varied between 15 and

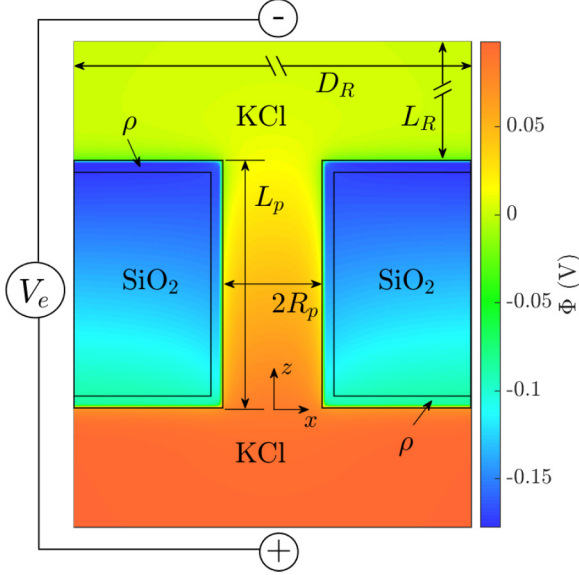


FIG. 1. A schematic diagram of our modeled nanopore structure with the electric potential in the background. (For this plot, the membrane charge is  $\rho = 0.4 e/\text{nm}^3$  and the bulk electrolyte concentration is  $C = 0.1 \text{ M}$ ).

100 nm. The reservoirs above and below the nanopore have dimensions which are much larger than the dimensions of the nanopore,  $L_R = 120 \text{ nm}$  and  $D_R = 280 \text{ nm}$ , to ensure that far away from the nanopore the electric potential reaches constant values. The difference between these values is equal to the electrolyte bias  $V_e = 100 \text{ mV}$  which is applied to generate the ionic flow through the nanopore. The 4-Å-thick layer on the surface of the  $\text{SiO}_2$  membrane is charged with the volume charge density  $\rho$ . In this work, we perform computations for two values of  $\rho$ :  $\rho = 0.4 e/\text{nm}^3$  and  $1.2 e/\text{nm}^3$  which correspond to the surface charge densities  $\sigma = 0.16 e/\text{nm}^2$  and  $0.48 e/\text{nm}^2$ , respectively.

To calculate the EOF fluid velocity and study its dependence on various system parameters, we first compute the electric potential  $\Phi(\vec{r})$  and electrolyte charge distribution, i.e., concentrations of chlorine and potassium ions,  $C_{Cl^-}(\vec{r})$  and  $C_{K^+}(\vec{r})$ , respectively, in our system. This is accomplished by solving Poisson-Nernst-Planck equations:

$$\nabla^2 \Phi = -\frac{e}{\epsilon_0 \epsilon_r} \rho(\vec{r}) \quad (1)$$

with

$$\rho(\vec{r}) = \begin{cases} \rho, & \text{in the 4-Å layer on the} \\ & \text{membrane surface,} \\ 0, & \text{everywhere else in the} \\ & \text{membrane,} \\ C_{K^+} - C_{Cl^-}, & \text{in the electrolyte,} \end{cases} \quad (2)$$

and

$$\nabla \cdot \left[ z_i \frac{e D_i}{k_B T} C_i \nabla \Phi + D_i \nabla C_i - \vec{v} C_i \right] = 0, \quad i = K^+, Cl^-. \quad (3)$$

Here  $e$  is the elementary charge,  $\epsilon_0$  is the permittivity of free space,  $\epsilon_r = 78$  is the relative permittivity of water,  $z_i = \pm 1$  are

the ionic charges of potassium and chlorine ions [15,21],  $T = 300 \text{ K}$  is the temperature of the system,  $\vec{v}$  is the EOF velocity, and  $D_i$  is the diffusion coefficient,  $D_{K^+} = 1.95 \times 10^{-9} \text{ m}^2/\text{s}$  and  $D_{Cl^-} = 2.03 \times 10^{-9} \text{ m}^2/\text{s}$ . The first two terms in the ionic fluxes (3) represent the electromigrative flux due to the applied electric field (drift current density) and diffusive flux, respectively, while the last term which depends on the fluid velocity describes the convective flux of ions due to the EOF.

The EOF through the nanopore is described via the Navier-Stokes equation for an incompressible fluid without the inertial term [22] as the Reynolds number for our nanopore geometry is  $\sim 10^{-3} - 10^{-4}$  depending on the pore's length:

$$\eta \nabla^2 \vec{v} = \nabla p - e(C_{K^+} - C_{Cl^-}) \nabla \Phi, \quad (4)$$

together with the continuity equation,

$$\nabla \cdot \vec{v} = 0, \quad (5)$$

where  $\eta = 10^{-3} \text{ Pa s}$  is the dynamic viscosity, and  $p$  is the total pressure. The last term on the right in Eq. (4) is the electric force responsible for the appearance of the electro-osmotic flow.

To get the velocity  $\vec{v}(\vec{r})$  of the EOF through the nanopore, Eqs. (1)–(5) were solved self-consistently with COMSOL<sup>®</sup> Multiphysics 5.1 on the axisymmetric two-dimensional domain (Fig. 1). A triangular finite element mesh with sizes varying from 0.35 Å on the membrane surface to 1.4 Å in the nanopore and 2.2 nm in the reservoirs and in the membrane was used in calculations. Small mesh sizes next to the membrane surface were required to capture very sharp variations in the electric potential for the larger membrane surface charge density. The simulations were terminated when the norm of the residual vector for the solution became smaller than  $10^{-6}$ .

The boundary conditions imposed for solving Eqs. (1)–(5) were as follows: The normal components of the ionic fluxes were set to zero at the nanopore-membrane interface and side reservoir walls while at the top and bottom walls of reservoirs the ionic concentration was maintained at its bulk value. The normal component of the electric field was set to zero at the side reservoir and membrane walls, while  $\Phi = V_e$  at the bottom and  $\Phi = 0$  at the top boundaries of the reservoir. For the Navier-Stokes equation, a no slip boundary condition ( $\vec{v} = 0$ ) was imposed at the nanopore-membrane interface while a slip boundary condition (the normal component of the velocity and its gradient are both zero) was used on the side walls of the reservoirs. At the top and bottom boundaries of the reservoirs, the pressure was set to zero together with the assumption that the fluid flow is normal to those boundaries.

For long cylindrical pores, the solution of the above system of equations for the fluid velocity is well known [20,23]. Within the Debye approximation for the electric potential (which is valid for  $\Phi \lesssim k_B T$ ) and assuming separability of  $\Phi(\vec{r})$  in  $z$  and  $x$  directions and no applied external pressure, the  $z$  component of the EOF velocity is given by

$$v_z(r) = -\frac{\epsilon_0 \epsilon_r E_z \Phi_0}{\eta} \left[ 1 - \frac{I_0(\kappa r)}{I_0(\kappa R_p)} \right], \quad (6)$$

where  $\kappa = (\epsilon_0 \epsilon_r k_B T / 2 C e^2)^{-1/2}$  is the inverse Debye length,  $C$  is the bulk electrolyte concentration (except where it is noted, all calculations are performed for  $C = 0.1 \text{ M}$ ),  $E_z$  is the

constant electric field along the central axis of the nanopore,  $I_n(x)$  is the modified Bessel function of the first kind of the  $n$ th order [24], and  $\Phi_0$  is the electric potential on the pore's surface which for zero applied electrolyte bias is equal to [25]

$$\Phi_0 = \frac{\sigma}{\epsilon_0 \epsilon_r \kappa} \frac{I_0(\kappa R_p)}{I_1(\kappa R_p)}. \quad (7)$$

For the two membrane charge densities considered in the present work,  $\Phi_0 = -40$  and  $-120$  meV, respectively, suggesting that the smaller charge density (barely) corresponds to the Debye approximation while for the larger one ( $0.48 e/\text{nm}^2$ ), this approximation, and consequently the above equation for  $v_z$ , cannot be used. However, as it is shown in the next section, Eq. (6) works well in our analytical model if  $\Phi_0$  is replaced with the potential difference  $\Delta\Phi$  between the surface and the center of the nanopore,  $\Delta\Phi = \Phi(R_p, L_p/2) - \Phi(0, L_p/2)$  (which is equal to  $-35$  and  $-78$  meV for our membrane charge values) provided that the ‘‘end effects’’ are also accounted for.

Note that Eq. (6) predicts that the fluid velocity reaches a maximum at the center of the pore. In the limit of a thin double layer ( $\kappa^{-1} \ll R_p$ ), Eq. (6) reduces to a constant value of  $v_z = \epsilon_0 \epsilon_r E_z \Phi_0 / \eta$  which is the classical Helmholtz-Smoluchowski result for the EOF fluid velocity [26,27].

### III. RESULTS AND DISCUSSION

We first checked the validity of the above numerical approach against the results of Eq. (6) and found very good agreement between the two for long nanopores and smaller surface charge densities as expected (see Appendix).

The computed EOF velocity contour plots with flow streamlines are shown in Fig. 2 for pore radii 5 and 10 nm and length of 25 nm. We see that within the nanopore, the direction of the fluid flow is along the pore's axis, as expected,

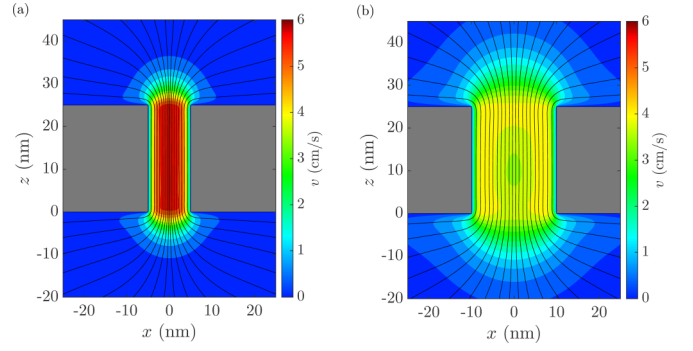


FIG. 2. Contour plots of the computed EOF velocity with streamlines for a nanopore with (a)  $R_p = 5$  nm and (b) 10 nm.

since it is where the electric potential changes most rapidly in the  $z$  direction (see Fig. 1), i.e., the electric field is the largest in magnitude. The radial component of the fluid velocity is only noticeable near the pore's inlet and outlet, and in those regions, the fluid flow extends over a distance of a few pore radii  $R_p$  away from the pore ends. We also observe the formation of a local *minimum* in the fluid velocity around the center of the pore with larger radius of 10 nm [Fig. 2(b)] while  $v$  remains maximal along the central axis of the nanopore when  $R_p = 5$  nm [Fig. 2(a)].

Figure 3 shows that the minimum appears and becomes deeper with decreasing length of the pore for a fixed  $R_p$ . The dashed and dotted curves in these plots correspond to the results given by Eq. (6), and one can immediately draw several observations from the comparison between the different types of curves: First, the velocities obtained from Eq. (6) with  $\Delta\Phi$  ( $\Phi_0$ ) exceed the numerically computed ones by as large as 40% (100%) particularly for  $\rho = 1.2 e/\text{nm}^3$ , and second, the fluid velocity  $v_z$  does not have a local minimum along

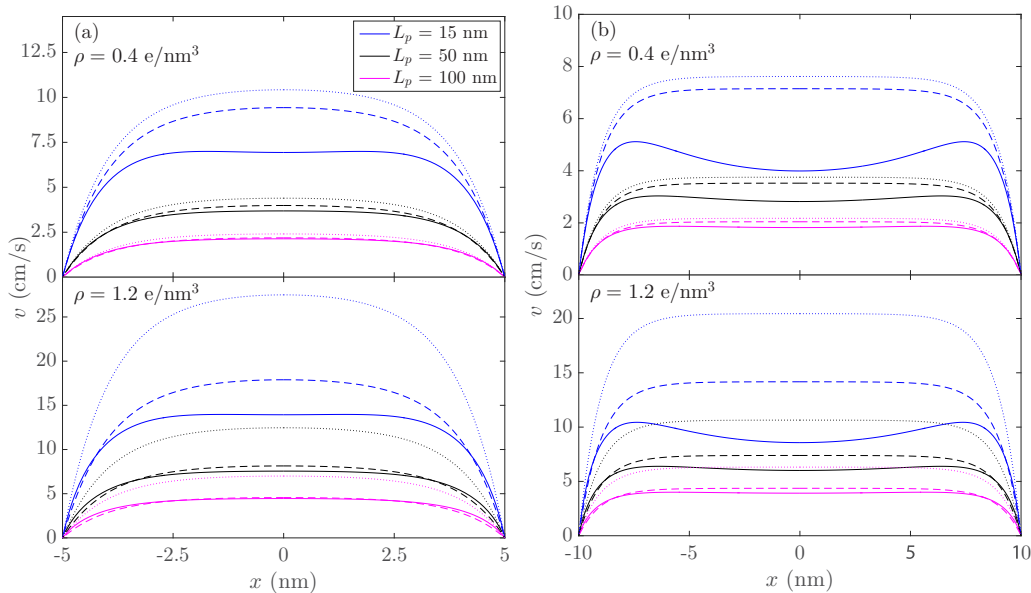


FIG. 3. Fluid velocity profile in  $x$  direction in the center of the pore for different nanopore lengths  $L_p$  and membrane charge densities: (a)  $R_p = 5$  nm and (b)  $R_p = 10$  nm. The solid curves are the results of the numerical simulations while the dashed (dotted) curves are the results of Eq. (6) with  $\Delta\Phi$  ( $\Phi_0$ ). For both dashed and dotted curves,  $E_z = V_e / (L_p + \alpha R_p)$  where values of parameter  $\alpha$  are given in text (see Sec. III for details).

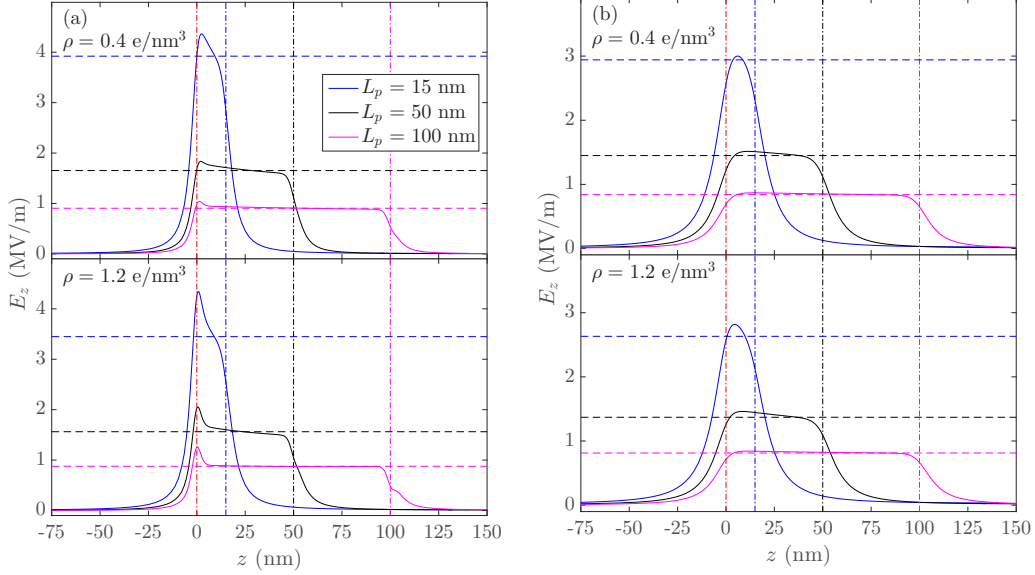


FIG. 4.  $z$  component of the electric field  $E_z$  along the central pore axis for a nanopore with (a)  $R_p = 5$  nm and (b)  $R_p = 10$  nm and different pore lengths. The horizontal dashed lines represent the values of the electric field as computed by  $E_z = V_e / (L_p + \alpha R_p)$  with  $\alpha$  given in the text, and the vertical dot-dashed lines show the location of the inlet ( $z = 0$ ) and outlet ( $z = 15$ ,  $z = 50$ , and  $z = 100$  nm) for each nanopore.

the central axis. As the pore becomes longer, the concave shape of the numerically computed velocity profile gradually disappears and velocity reaches a maximum value along the central axis of the pore, qualitatively similar to the  $v_z$  profile predicted by Eq. (6). Note that the concave shape of the fluid velocity was previously observed in numerical calculations of the EOF through long nanopores (see, e.g., Ref. [28]). However, in what follows we strive to provide a qualitative explanation for its appearance as well as to devise a way to rectify Eq. (6) so that values of  $v_z$  agree with the numerically computed EOF velocities.

One of the reasons for the apparent disagreement between the numerically computed EOF velocity and the one determined by Eq. (6) is the magnitude of the electric field  $E_z$  in the  $z$  direction due to the applied bias  $V_e$ . A conventional argument that  $V_e$  changes linearly over the pore's length leads to  $E_z = V_e / L_p$  since usually  $L_p \gg \kappa^{-1}$ . However, as can be seen from the electric potential distribution shown in Fig. 1, the potential changes over distances extending a few  $R_p$ 's away from the nanopore's ends. This is because inside the nanopore, the positive and negative ionic charges do not fully compensate each other (due to the presence of the membrane surface charge) and the nanopore as a whole has a nonzero electric charge. In this case, the electric field inside the pore can be approximated as [29,30]

$$E_z = \frac{V_e}{L_p + \alpha R_p} \quad (8)$$

with  $\alpha$  being a numerical parameter dependent on the nanopore radius, surface charge, and bulk electrolyte concentration values.

The overall form of Eq. (8) can be justified by representing the nanopore region in terms of the nanopore and two access sections. Using the nanopore and access resistances with the pore diameter modified by the surface charge [31] and substituting them into the equation for the potential drop along

the nanopore length [25], one can find that parameter  $\alpha$  in the above equation can be expressed as

$$\alpha = \frac{\pi}{2} \frac{1 + \text{Du}}{1 + \text{Du}/4}, \quad (9)$$

where  $\text{Du} \approx |\sigma| / CR_p$  is the Dukhin number [31]. For our nanopore radii  $R_p = 5(10)$  nm, this gives  $\alpha \approx 2.1(1.9)$  for  $\rho = 0.4 e/\text{nm}^3$  and 2.9 (2.3) for  $\rho = 1.2 e/\text{nm}^3$  which results in excellent agreement between the numerically computed electric fields and the values given by Eq. (8), see Fig. 4, as well as with other calculations of the electric field in charged nanopores [29,30].

However, the main reason for the concave shape of the velocity profile in the fluid flow through finite length nanopores is the presence of the self-induced pressure drop  $P$  along the pore shown in Fig. 5 for the larger membrane charge of  $1.2 e/\text{nm}^3$  (results for the smaller charge are analogous and are not shown). The pressure changes approximately linearly along the pore's axis [32,33]; the deviations from linearity are due to the concentration polarization effects [34], i.e., the electric force in the Navier-Stokes equation (4) is not constant in the  $z$  direction but rather exhibit a slight variation due to the changing ionic concentration along the pore's axis. This effect diminishes as pore's radius increases which is manifested by a more linear pressure drop in Fig. 5(b) vs Fig. 5(a).

This pressure drop appears due to the fluid flow expansion or contraction near the pore's outlet or inlet or in other words, it is the result of the finite length of the nanopore: Outside of the nanopore's outlet, the fluid velocity decreases with the distance away from the pore (streamlines diverge, see Fig. 2). Since the fluid is incompressible, one can write for its velocity outside the pore [35]

$$v(R) \approx \frac{Q}{2\pi R^2}, \quad (10)$$

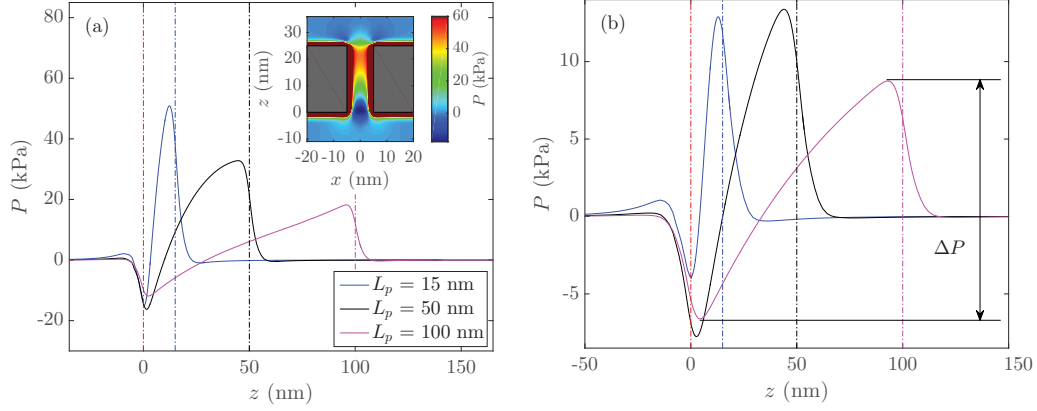


FIG. 5. Induced pressure  $P$  along the central pore axis for nanopores of different lengths and (a)  $R_p = 5$  nm, (b)  $R_p = 10$  nm ( $\rho = 1.2 e/\text{nm}^3$ ). The total pressure drop  $\Delta P$  is defined as difference between the maximum and minimum pressure values. The vertical dot-dashed lines show the location of the inlet ( $z = 0$ ) and outlet ( $z = 15$ ,  $z = 50$ , and  $z = 100$  nm) for each nanopore. The inset in (a) shows distribution of the pressure in the fluid.

where  $R$  is the distance between the pore's exit and observation point, and  $Q$  is the volumetric flow rate. This results in the appearance of the fluid friction force between the layers of the fluid and as such, the pressure is induced to maintain the flow. We can estimate the induced pressure  $\delta P$  by equating it to the fluid friction force per unit area [36] which leads to  $\delta P = (1/2)\beta\eta Q/R_p^3$ . Here we introduced a variational parameter  $\beta$  to relate  $R$  and  $R_p$  since the fluid velocity decays appreciably over a few  $R_p$ 's away from the pore. Note that because we consider the fluid flow outside the nanopore,  $\beta$  does not depend on  $L_p$ .

Near the pore's inlet, the situation is analogous but the pressure there drops below the fixed external value to compensate for the contraction of the fluid streamlines. Assuming that this decrease in pressure is the same in magnitude as its increase near the pore's outlet, for the total pressure change along the pore's length, one can thus write

$$\Delta P = \beta \frac{\eta Q}{R_p^3}. \quad (11)$$

The fluid flow due to the induced pressure contributes to the net EOF, so that Eq. (6) has to be modified to account for its effect [32]:

$$v_z(r) = -\frac{R_p^2 \Delta P}{4\eta L_p} \left(1 - \frac{r^2}{R_p^2}\right) - \frac{\epsilon_0 \epsilon_r E_z \Delta \Phi}{\eta} \left[1 - \frac{I_0(\kappa r)}{I_0(\kappa R_p)}\right], \quad (12)$$

where for simplicity we assumed that the pressure-induced flow is parabolic (Poiseuille flow) in the radial direction and that the pressure changes linearly along the pore (see Fig. 5).

To determine the value of  $\beta$ , we computed the pressure drop along the pore from the data in Fig. 5 and compared it with  $\Delta P$  given by Eq. (11) in which  $Q$  was obtained by integrating Eq. (12) over the pore's cross sectional area which leads to

$$\Delta P = -\frac{8V_e}{R_p^2} \frac{\Pi}{\alpha/2 + \Pi} \frac{\epsilon_0 \epsilon_r \Delta \Phi}{1 + 16\Pi/\pi\beta} \left[1 - \frac{2I_1(\kappa R_p)}{\kappa R_p I_0(\kappa R_p)}\right], \quad (13)$$

where  $\Pi$  is the aspect ratio of the nanopore,  $\Pi = L_p/(2R_p)$ , and we also used  $E_z = V_e/(L_p + \alpha R_p)$ . The values of the pressure drop vs the aspect ratio of the nanopore are shown in Fig. 6 where one can see that the agreement between the numerically computed and approximate values of  $\Delta P$  is quite good when  $\beta = 1.75$ , particularly for pores with  $\Pi \gtrsim 2$ . The pressure reaches maximum at  $\Pi \sim 1$  and decreases at smaller and larger values of the aspect ratio. The deviations at smaller aspect ratios are likely due to the fact that the EOF is not yet established in short pores (for the pressure driven flow, the flow becomes fully developed when  $L_p \gtrsim R_p$  [32]), i.e., the fluid velocity is smaller than the one given by Eq. (6). In the opposite limit of the long pores  $L_p \gg R_p$ ,  $\Delta P \propto L_p^{-1}$  due to the decreasing electric field magnitude.

With the value of  $\beta$  thus fixed, we can now find the fluid velocity profile in the radial direction as given by Eqs. (12) and (13). In Fig. 7, we replot the numerically computed EOF

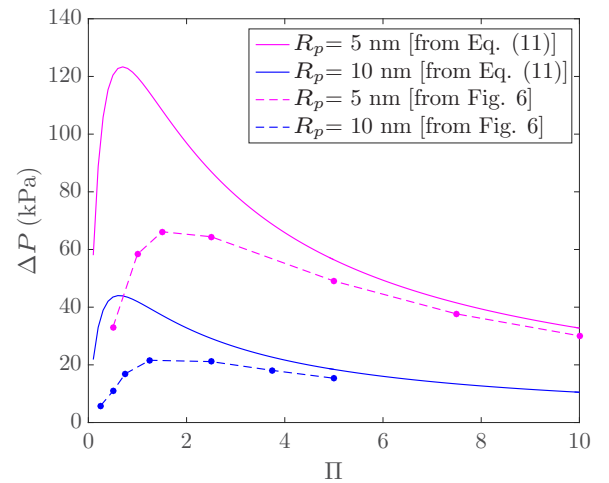


FIG. 6. Induced pressure drop  $\Delta P$  vs aspect ratio of the pore  $\Pi = L_p/(2R_p)$  for  $\rho = 1.2 e/\text{nm}^3$ . Dots connected by dashed lines are the results of calculations, solid curves are the result of Eq. (13) with  $\beta = 1.75$ . Note that the same  $\beta$  is used for both  $R_p = 5$  and 10 nm.

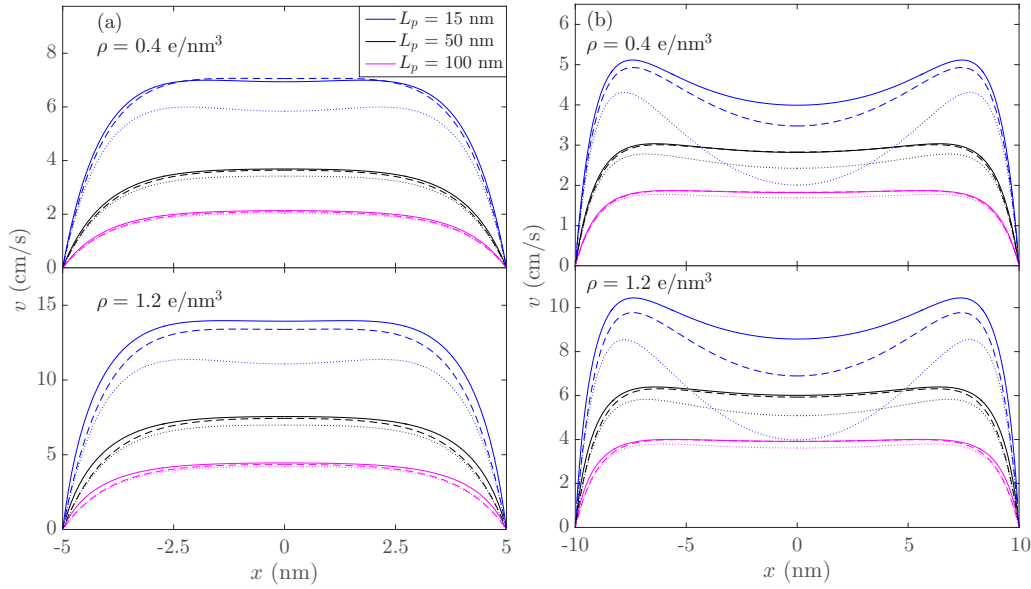


FIG. 7. Same as in Fig. 3 but with dashed lines from Eqs. (12) and (13) with  $\beta = 1.75$  and dotted lines with  $\beta = 3$ .

velocities (solid curves) but compare them now with results of Eq. (12) (dashed curves): The agreement between two sets of data is very good (unlike Fig. 3) for all studied nanopores demonstrating the importance of the induced pressure effects on the EOF through the nanopores in thin and ultrathin membranes.

Note that an equation for the pressure drop similar to Eq. (11) but with fixed  $\beta = 3$  was derived for the pressure-driven flow through the circular orifice in the infinitely thin screen [37,38]. It was later utilized for the description of the end effects in the pressure driven flow through the finite length channels [39], where a good agreement between the exact numerical and approximate results was found. However, as can be seen from the dotted curves in Fig. 7, the parameter

$\beta = 3$  is much too large to provide a good agreement with the numerically computed EOF fluid velocities for our nanopores [25,40].

Finally, in Fig. 8, we show how the electrolyte concentration  $C$  affects the fluid velocity. One can see from these plots that the dependence of  $v$  on  $C$  has a nonmonotonic character for pores with  $R_p = 5$  nm: Fluid velocity at the pore's center first increases with increasing electrolyte concentration and then decreases. This can be easily understood by analyzing concentration dependence of  $v_z(r)$  in Eq. (12). The electric potential on the membrane surface  $\Phi_0$  [Eq. (7)] monotonically decreases with  $C$  [13]. However, for small electrolyte concentrations and  $R_p = 5$  nm, the velocity at the center of the pore has not yet reached Helmholtz-Smoluchowski

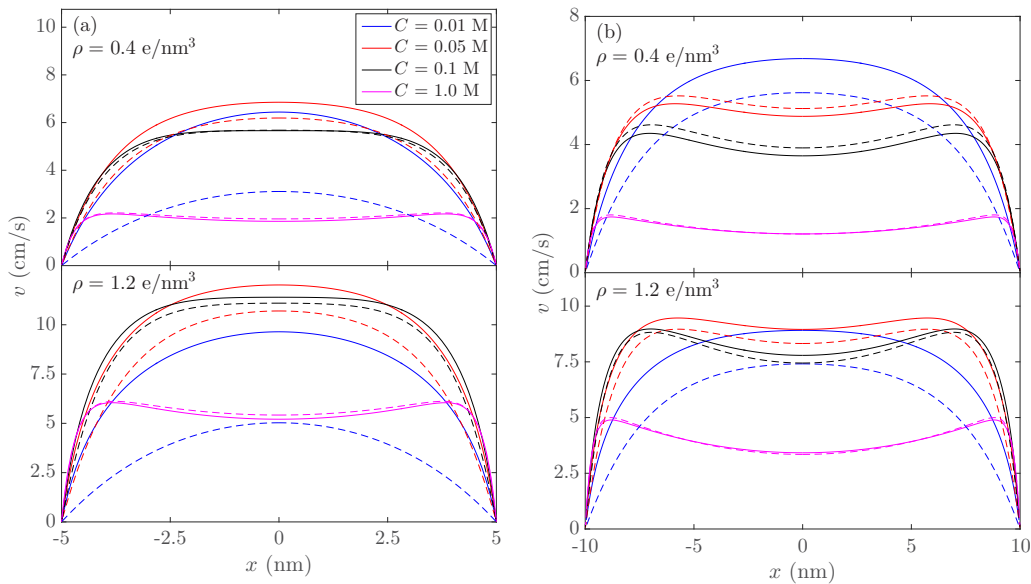


FIG. 8. The fluid velocity profile in  $x$  direction at the center of the nanopore of length  $L_p = 25$  nm for different bulk electrolyte concentrations  $C$ : (a)  $R_p = 5$  nm and (b) 10 nm. The dashed lines are the results of Eq. (12).

saturation limit, that is, the electric double layers from opposite sides of the pore overlap, and overall,  $v_z$  increases with  $C$ . When Helmholtz-Smoluchowski limit is reached, the only dependence on concentration in Eq. (12) is through  $\Phi_0$ , and thus,  $v_z$  decreases. For  $R_p = 10$  nm, the velocity decreases with  $C$  [Fig. 8(b)] because in this case  $\kappa R_p \gg 1$  in the studied range of concentrations.

In the same plots, we also compare the numerically computed velocities with the ones given by Eq. (12). One can see that the agreement is very good for all concentrations except for the lowest one,  $C = 10$  mM, when the approximate calculations significantly underestimate the numerical results. The main reason for this is a strong  $z$  dependence of the electric field in and around the nanopore as compared to the ones shown in Fig. 4 and used in Eqs. (12) and (13). At low electrolyte concentrations, the electric field varies greatly along the nanopore length (there is a lot of the electric field “leakage” from the top and bottom membrane surfaces into the nanopore) and it is hard to ascribe just one value for it for the whole nanopore length. In other words, at low electrolyte calculations and/or nanopore aspect ratios, the full scale numerical calculations are better suited for the description of the EOF.

#### IV. CONCLUSION

In this paper, we theoretically studied the EOF through nanopores of variable radii in thin and ultrathin solid state membranes for different nanopore dimensions, electrolyte concentrations and membrane charges. Numerical analysis of the EOF fluid velocity is performed via self-consistent solution of the Poisson-Nernst-Planck and Navier-Stokes equation in two dimensions accounting for large fluid reservoirs above and below nanopore. These large domains, while greatly increasing the computational cost, are necessary to properly account for the end effects around the inlet and outlet of the nanopore. We found that the computed fluid velocity profiles are not only different by as much as 100% from the results predicted by classical equations derived for infinitely long capillaries, but that they also develop a concave shape for sufficiently wide and/or short nanopores. This behavior stems from the presence of the self-induced pressure gradient along the nanopore due to the flow expansion or contraction near ends of the pore as well as the reduction of the electric field inside the nanopore due to the increase of the effective nanopore length caused by the access resistance and the membrane surface charge. Based on the classical model for the EOF in long pores, we also developed a simple analytical model incorporating these effects, and found that its results are in a good agreement with those of the numerical calculations.

Although in this work we concentrate on thin and ultrathin membranes, our results concerning the magnitude of the

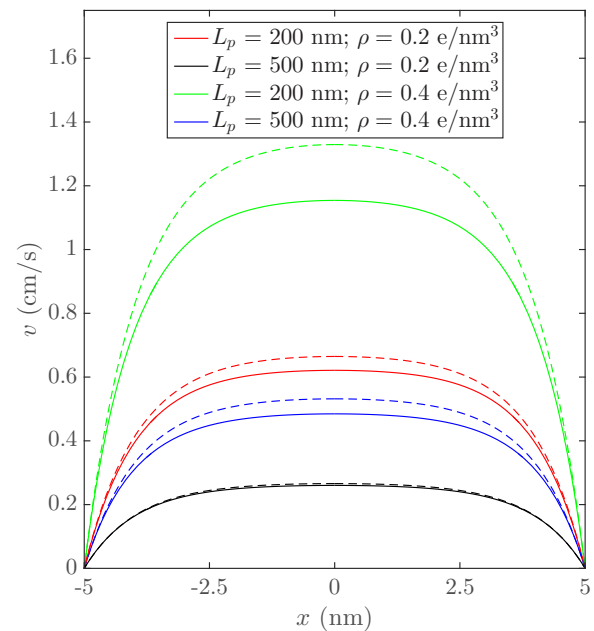


FIG. 9. The fluid velocity profile in  $x$  direction at the center of the nanopores with  $R_p = 5$  nm and varying length  $L_p$  (solid curves). The dashed lines are the results of Eq. (6) with  $E_z = V_e/L_p$ .

induced pressure and how it affects the EOF velocity are also applicable for other pore dimensions as Eq. (13) does not depend explicitly on the nanopore length. In this respect, they can be used to predict and quantitatively estimate the induced pressures near the nanopore inlet or outlet and their effect, for example, on translocation of “deformable” particles through the nanoporous membranes [33] and other nanofluidic devices.

#### ACKNOWLEDGMENTS

We are grateful to I. A. Jou for helpful discussions. This work was supported by NSF CAREER Award No. DMR-1352218.

#### APPENDIX: VALIDATION OF THE APPROACH

To check the validity of our numerical approach, we computed the EOF velocity in very long nanopores where numerical results are expected to approach the values given by Eq. (6) for smaller surface charge densities when the Debye approximation is valid. As results in Fig. 9 show, this is indeed the case: For 200-nm-long pores, the relative difference between numerically computed and approximate values of the velocity is about 15(7)% for  $\rho = 0.4(0.2) e/nm^3$  while for a 500-nm-long nanopore, the difference is  $\sim 10(2)$  %.

- [1] C. C. Striemer, T. R. Gaborski, J. L. McGrath, and P. M. Fauchet, *Nature (London)* **445**, 749 (2007).  
 [2] S. Howorka and Z. Siwy, *Chem. Soc. Rev.* **38**, 2360 (2009).

- [3] I. Vlassiuk, P. Y. Apel, S. N. Dmitriev, K. Healya, and Z. S. Siwy, *Proc. Natl. Acad. Sci. USA* **106**, 21039 (2009).  
 [4] A. Oukhaled, L. Bacri, M. Pastoriza-Gallego, J.-M. Betton, and J. Pelta, *ACS Chem. Biol.* **7**, 1935 (2012).

- [5] B. N. Miles, A. P. Ivanov, K. A. Wilson, F. Dogan, D. Japrun, and J. B. Edel, *Chem. Soc. Rev.* **42**, 15 (2013).
- [6] L. Movileanu, *Protein Pept. Lett.* **21**, 235 (2014).
- [7] M. Muthukumar, C. Plesa, and C. Dekker, *Phys. Today* **68**(8), 40 (2015).
- [8] B. M. Venkatesan and R. Bashir, *Nat. Nanotechnol.* **6**, 615 (2011).
- [9] L. Luo, S. R. German, W.-J. Lan, D. A. Holden, T. L. Mega, and H. S. White, *Annu. Rev. Anal. Chem.* **7**, 513 (2014).
- [10] A. McMullen, H. W. de Haan, J. X. Tang, and D. Stein, *Nat. Commun.* **5**, 4171 (2014).
- [11] Y. Qiu, P. Hinkle, C. Yang, H. E. Bakker, M. Schiel, H. Wang, D. Melnikov, M. Gracheva, M. E. Toimil-Molares, A. Imhof, and Z. S. Siwy, *ACS Nano* **9**, 4390 (2015).
- [12] M. Tsutsui, Y. He, K. Yokota, A. Arima, S. Hongo, M. Taniguchi, T. Washio, and T. Kawai, *ACS Nano* **10**, 803 (2016).
- [13] M. Firmkes, D. Pedone, J. Knezevic, M. Döblinger, and U. Rant, *Nano Lett.* **10**, 2162 (2010).
- [14] A. M. Berezhkovskii and S. M. Bezrukov, *Biophys. J.* **88**, L17 (2005).
- [15] I. A. Jou, D. V. Melnikov, A. Nadtochiy, and M. E. Gracheva, *Nanotechnology* **25**, 145201 (2014).
- [16] T. R. Gaboriski, J. L. Snyder, C. C. Striemer, D. Z. Fang, M. Hoffman, P. M. Fauchet, and J. L. McGrath, *ACS Nano* **4**, 6973 (2010).
- [17] M. Wanunu, T. Dadoosh, V. Ray, J. Jin, L. McReynolds, and M. Drndić, *Nat. Nanotechnol.* **5**, 807 (2010).
- [18] M. Tsutsui, S. Hongo, Y. He, M. Taniguchi, N. Gemma, and T. Kawai, *ACS Nano* **6**, 3499 (2012).
- [19] U. M. B. Marconi and S. Melchionna, *Langmuir* **28**, 13727 (2012).
- [20] C. L. Rice and R. Whitehead, *J. Phys. Chem.* **69**, 4017 (1965).
- [21] S. Qian and Y. Ai, *Electrokinetic Particle Transport in Micro-/Nanofluidics: Direct Numerical Simulation Analysis* (CRC, Boca Raton, FL, 2012).
- [22] J. G. Santiago, *Anal. Chem.* **73**, 2353 (2001).
- [23] A. Piruska, M. Gong, J. V. Sweedler, and P. W. Bohn, *Chem. Soc. Rev.* **39**, 1060 (2010).
- [24] M. Abramowitz, *Handbook of Mathematical Functions, With Formulas, Graphs, and Mathematical Tables* (Dover, New York, 1974).
- [25] J. D. Sherwood, M. Mao, and S. Ghosal, *Langmuir* **30**, 9261 (2014).
- [26] H. Helmholtz, *Ann. Phys.* **243**, 337 (1879).
- [27] M. von Smoluchowski, *Handbuch der Elektrizität und des Magnetismus* (Barth, Leipzig, 1914), Vol. 2, pp. 366–428.
- [28] L. M. Innes, C.-H. Chen, M. Schiel, M. Pevarnik, F. Haurais, M. E. Toimil-Molares, I. Vlassiouk, L. Theogarajan, and Z. S. Siwy, *Anal. Chem.* **86**, 10445 (2014).
- [29] J. Nakane, M. Akeson, and A. Marziali, *Electrophoresis* **23**, 2592 (2002).
- [30] J. Getpreecharsawas, J. L. McGrath, and D. A. Borkholder, *Nanotechnology* **26**, 045704 (2015).
- [31] C. Lee, L. Joly, A. Siria, A.-L. Biance, R. Fulcrand, and L. Bocquet, *Nano Lett.* **12**, 4037 (2012).
- [32] Y. Zhang, X.-J. Gu, R. W. Barber, and D. R. Emerson, *J. Colloid Interface Sci.* **275**, 670 (2004).
- [33] M. Pevarnik, M. Schiel, K. Yoshimatsu, I. V. Vlassiouk, J. S. Kwon, K. J. Shea, and Z. S. Siwy, *ACS Nano* **7**, 3720 (2013).
- [34] Q. Pu, J. Yun, H. Temkin, and S. Liu, *Nano Lett.* **4**, 1099 (2004).
- [35] C. T. A. Wong and M. Muthukumar, *J. Chem. Phys.* **126**, 164903 (2007).
- [36] L. D. Landau and E. M. Lifshitz, *Fluid Mechanics*, 2nd ed. (Pergamon Press, Oxford, 1987).
- [37] R. Roscoe, *Phil. Mag.* **40**, 338 (1949).
- [38] H. Hasimoto, *J. Phys. Soc. Jpn.* **13**, 633 (1958).
- [39] Z. Dagan, S. Weinbaum, and R. Pfeffer, *J. Fluid Mech.* **115**, 505 (1982).
- [40] R.-J. Yang, T.-I. Tseng, and C.-C. Chang, *J. Micromech. Microeng.* **15**, 254 (2005).